Article

Solid-State Calcium-Ion Diffusion in $Ca_{1.5}Ba_{0.5}Si_5O_3N_6$

Yu Chen, Christopher J. Bartel, Maxim Avdeev, Ya-Qian Zhang, Jue Liu, Peichen Zhong, Guobo Zeng, Zijian Cai, Haegyeom Kim, Huiwen Ji,* and Gerbrand Ceder*

Cite This: https://doi.org/10.1021/acs.chemmater.1c02923

Read Online

ACCESS | ⬛ Metrics & More | 📖 Article Recommendations | 🆂🅸 Supporting Information

ABSTRACT: Rechargeable batteries based on multivalent working ions are promising candidates for next-generation high-energy-density batteries. Development of these technologies, however, is largely limited by the low diffusion rate of multivalent ions in solid-state materials, thereby necessitating a better understanding of the design principles that control multivalent-ion mobility. Here, we report $Ca_{1.5}Ba_{0.5}Si_5O_3N_6$ as a potential calcium solid-state conductor and investigate its Ca migration mechanism by means of ab initio computations and neutron diffraction. This compound contains partially occupied Ca sites in close proximity to each other, providing a unique mechanism for Ca migration. Nuclear density maps obtained with the maximum entropy method from neutron powder diffraction data provide strong evidence for low-energy percolating one-dimensional pathways for Ca-ion migration. Ab initio molecular dynamics simulations further support a low Ca-ion migration barrier of ~400 meV when Ca vacancies are present and reveal a unique "vacancy-adjacent" concerted ion migration mechanism. This work provides a new understanding of solid-state Ca-ion diffusion and insights into the future design of novel cation configurations that utilize the interactions between mobile ions to enable fast multivalent-ion conduction in solid-state materials.
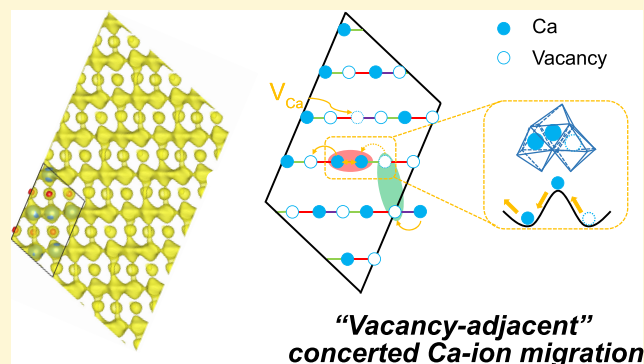
"Vacancy-adjacent" concerted Ca-ion migration

INTRODUCTION

Rechargeable batteries based on multivalent ions (e.g., Mg^{2+}, Ca^{2+}, Zn^{2+}) have the potential to overcome the high cost and energy-density limits of Li-ion batteries.[1−3] Calcium is especially attractive owing to its nontoxicity, abundance, and low standard reduction potential (−2.78 V vs standard hydrogen electrode) comparable to that of lithium.[4,5] Although Ca^{2+} doubles the carrier charge relative to Li^+, it has a reasonably large size similar to Na^+, resulting in a similar charge density as Li^+. The less polarizing character of Ca^{2+} compared with those of other divalent cations (e.g., Mg^{2+}) is beneficial for the ion diffusion kinetics in both cathodes and electrolytes.[4,6,7]

However, the development of Ca-battery technology is still in a nascent stage. Identifying solid-state materials that can readily host and transport Ca^{2+} and elucidating the underlying Ca^{2+} migration mechanism are crucial steps toward the development of solid-state electrolytes and intercalation electrodes. In fact, the limited mobility of Ca^{2+} is one of the major obstacles in cathode design. Most proposed Ca-hosting transition-metal (TM) compounds, e.g., α-V_2O_5,[8] Ca cobaltites,[9] TiS_2,[10] perovskite-$CaMO_3$,[11] and marokite-$CaMn_2O_4$,[12] have density functional theory (DFT)-calculated Ca^{2+} migration barriers larger than 650 meV and thus are not considered viable Ca cathode materials. Recently, Park et al. reported layered $CaCo_2O_4$ as a potential Ca cathode with a remarkably low calculated migration barrier of 320 meV; however, Ca^{2+}

transport in this material has not yet been demonstrated experimentally.[13] The sluggish Ca^{2+} transport kinetics also poses problems when a solid electrolyte interphase (SEI) layer forms on the Ca metal anode.[14−16] Understanding the design principles that affect Ca^{2+} mobility is therefore a key step for further development of Ca batteries.

Here, we target Ca solid-state conductors with low Ca migration barriers, which promise superior mechanical and thermal stability compared with conventional liquid electrolytes. In the 1980s−1990s, Seevers et al. reported a Ca-ion conductivity of 3.6×10^{-2} S/cm at 300 °C in β''-Al_2O_3.[17] Nomura et al. studied NASICON-type $CaZr_4(PO_4)_6$ and reported a Ca-ion conductivity of 1.4×10^{-6} S/cm at 800 °C with a measured migration barrier of 146 kJ/mol (i.e., 1.51 eV).[18] Since then, however, no substantial progress in Ca solid-state conductors has been made, in sharp contrast with numerous Mg solid-state conductors that have been investigated (e.g., NASICON-type $MgZr_4(PO_4)_6$,[19−21] complex hydride $Mg(BH_4)(NH_2)$,[22,23] and chalcogenide spinel $MgSc_2Se_4$[24]).

Recently, Lazoryak and co-workers investigated Ca-ion conduction in $Ca_{10.5-x}Pb_x(VO_4)_7$ whitlockites showing an ionic conductivity of 10^{-4} S/cm at 800 K but with measured migration barriers that were rather high, about 1.3−1.5 eV.[25,26] Koettgen et al. predicted $CaB_{12}H_{12}$ as a potential Ca solid-state conductor;[27] however, its calculated migration barrier, 650 meV, is still much higher than those reported in Li and Mg superionic solid-state conductors (typically lower than 400 meV).[24,28,29] Therefore, much effort is still needed to discover new materials with structures that enable low-barrier Ca migration.

It has been demonstrated that mobile ions occupying high-energy sites can potentially activate a concerted migration mechanism with a low migration barrier.[30] Such configurations that place mobile ions in energetically unfavorable crystallographic sites are typically stabilized by strong Coulomb interactions from nearby mobile ions. With that in mind, we identified and synthesized a promising material $Ca_{1.5}Ba_{0.5}Si_5O_3N_6$ (CBSON) with a desirable Ca^{2+} configuration to unlock the concerted migration mechanism. This compound was first reported by Park et al. as a phosphor material.[31,32] In its structure, Ca^{2+} partially occupies three crystallographically distinct sites in the same layer with extremely short distances (1.727−2.077 Å) between the neighboring Ca sites, suggesting the potential for concerted Ca^{2+} migration. To probe the Ca diffusion in CBSON and identify possible migration pathways, we constructed nuclear density maps by applying the maximum entropy method (MEM) to neutron powder diffraction. This analysis provides clear evidence of percolating 1D chains of Ca nuclear density maxima indicative of potential pathways for Ca-ion conduction. We further used ab initio molecular dynamics (AIMD) simulations to probe the Ca^{2+} diffusivity in CBSON, revealing a Ca migration barrier of ~400 meV and a unique "vacancy-adjacent" concerted ion migration mechanism. This work suggests that the interactions between mobile ions can be significant for multivalent-ion systems, and designing proper cation configurations to better utilize the ion−ion interaction is vital to achieve high ion mobility. The large cation size of Ca^{2+} imposes additional constraints (e.g., steric effects) on cation−cation interactions that need to be considered and, in this work, leads to the posited "vacancy-adjacent" concerted ion migration mechanism.

METHODS

Synthesis. $Ca_{1.5}Ba_{0.5}Si_5O_3N_6$ (CBSON) was synthesized by a solid-state method. CaO (Sigma-Aldrich, anhydrous, ≥99.99%), $Ca(OH)_2$ (Sigma-Aldrich, 99.995%), BaO (Alfa Aesar, 99.5%), Si_3N_4 (Sigma-Aldrich, ≥99.9%), and SiO_2 (Sigma-Aldrich, 99.5%) were used as precursors. Both CaO and $Ca(OH)_2$ were used as Ca sources with a molar ratio of 1:1. All of the precursors were stoichiometrically mixed in ethanol (except that 10% excess $Ca(OH)_2$ was added to compensate for possible loss during synthesis) in a 50 mL WC jar with five 10 mm diameter WC balls using a Retsch PM200 planetary ball mill at 250 rpm for 12 h. The precursors were then dried overnight in a 70 °C oven and pressed into pellets of 13 mm in diameter under an axial pressure of 5 metric tons for 2 min. Two or three precursor pellets (~1 g each) were placed in a glassy carbon crucible and sintered at 1400 °C for 5 h under a N_2 flow, with the same heating and cooling rates of 1 °C/min above 800 °C and 5 °C/min below 800 °C. After calcination, the pellets were transferred to a glovebox and manually ground into fine powders. Prior to densifying the pellet, the as-synthesized CBSON powders were ball-milled again at 300 rpm for 12 h to decrease the particle size. The jars were sealed with safety closure clamps in an Ar-filled glovebox. Both the product and precursors (i.e., SiO_2 and Si_3N_4) have high hardness as a result of their Si tetrahedral networks. Therefore, during mixing or ball-milling, the use of a high-hardness material (e.g., WC) as the milling media is necessary to avoid abrasive wear and contamination (Figure S2). Then, the ball-milled CBSON powders were pressed into pellets of 6 mm in diameter under an axial pressure of 2 metric tons for 2 min in a glovebox. Three pellets (~0.2 g each) were placed in a glassy carbon crucible and covered with the same mother powder and then sintered at 1200, 1300, or 1400 °C, respectively, for 5 h under a N_2 flow. The heating and cooling rates were the same as those used in the first calcination step.

Compositional, Structural, and Morphological Characterization. Elemental analysis was performed by Galbraith Laboratories, Inc. using inductively coupled plasma optical emission spectroscopy for the Ca, Ba, and Si species. X-ray diffraction (XRD) patterns of the as-synthesized compounds were obtained using a Rigaku MiniFlex 600 diffractometer equipped with a Cu source. High-angle annular dark-field scanning transmission electron microscopy (HAADF-STEM) and energy-dispersive X-ray spectroscopy (EDS) mapping were performed on an FEI TitanX 60-300 microscope equipped with a Bruker windowless EDS detector at an acceleration voltage of 300 kV at the Molecular Foundry at Lawrence Berkeley National Lab (LBNL). Scanning electron microscopy (SEM) images were obtained using a Zeiss Gemini Ultra-55 analytical field-emission scanning electron microscope at the Molecular Foundry at LBNL.

Neutron Powder Diffraction. Time-of-flight (TOF) neutron powder diffraction experiments at 290 K were performed at the Spallation Neutron Source at Oak Ridge National Laboratory on the Nanoscale Ordered Materials Diffractometer.[33,34] The data were analyzed by Rietveld refinement[35] using the TOPAS v6 software package.[36] TOF were converted to d-spacing using a second-order polynomial $TOF = ZERO + DIFC \times d + DIFA \times d^2$, where ZERO is a constant, DIFC is the diffractometer constant, and DIFA is an empirical term to correct for sample displacements and absorption-induced peak shifts. For low-resolution banks, a back-to-back exponential function convoluted with a symmetrical pseudo-Voigt function was used to describe the peak profile. For high-resolution backscattering banks (banks 4 and 5), the moderator-induced line profile was modeled using a modified Ikeda−Carpenter−David function.[37] Lorenz factor is accounted by multiplying d^4. Neutron powder diffraction measurements at 3 and 475 K with a wavelength of 2.4395 Å were performed on the high-resolution powder diffractometer ECHIDNA at ANSTO in Australia.[38] Data analysis using MEM was performed using RIETAN-FP[39] and Dysnomia[40] codes. Structure visualization was performed with VESTA.[41]

DFT Calculations. DFT using the projector-augmented wave (PAW) method[42,43] as implemented in the Vienna ab initio simulation package (VASP)[44,45] was used for all of the calculations. Calculations to assess the thermodynamic stability, electrochemical stability, and defect formation energies were performed using the strongly constrained and appropriately normed (SCAN) meta-generalized gradient approximation (meta-GGA) density functional,[46] which was recently shown to be more accurate for structure and coordination prediction.[47,48] A plane-wave energy cutoff of 520 eV, at least 1000 k-points per reciprocal atom, and convergence criteria of 10^{-6} eV for electronic optimizations and 10^{-5} eV for ionic optimizations were used. The pseudopotential method was used with Ca $3s^23p^64s^2$, Ba $5s^25p^66s^2$, Si $3s^23p^2$, O $2s^22p^4$, and N $2s^22p^3$ electrons treated as valence.

CBSON was calculated with a $1 \times 1 \times 2$ supercell with the partially occupied Ca sites ordered in the configuration found to have the lowest energy after sampling various orderings (alternating stripes of Ca and V_{Ca} along the a axis, resulting in alternating Ca and V_{Ca} along the $a−c$ plane).

The thermodynamic and electrochemical stabilities were assessed using the convex-hull approach[49] against all unique entries in the Ca−Ba−Si−O−N chemical space in Materials Project[50] with a reported energy above the hull of ≤25 meV/atom. Electrochemical stability was evaluated using the grand potential phase diagram approach[51] on the same set of compounds in a system open to exchange with Ca.

Following ref 52, the defect formation energies for each defect X, $\Delta E_f[X]$, were calculated as
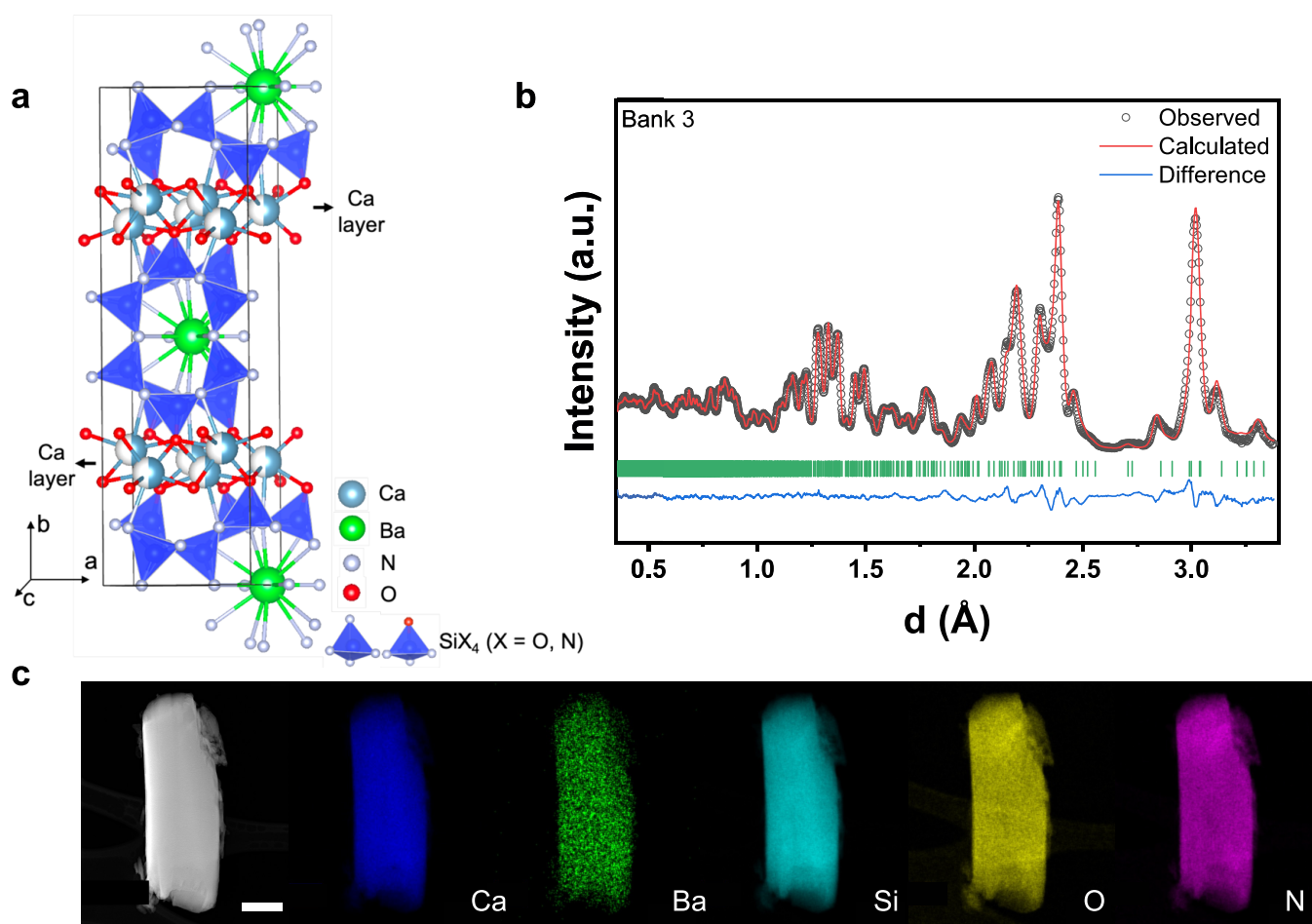
Figure 1. (a) Crystal structure of CBSON with partially occupied Ca sites. (b) Time-of-flight NPD pattern (bank 3) at 290 K and the corresponding Rietveld refinement of CBSON. The experimental data are shown as black circles, the red line is the calculated pattern, and the difference profile is shown in blue underneath. The calculated positions of the Bragg reflections are indicated by green vertical tick marks. (c) HAADF image of a representative CBSON particle and corresponding EDS mapping acquired from STEM. Scale bar, 200 nm.

$$\Delta E_f[X] = \Delta H_X - \Delta H_0 - \sum_i (n_{i,X} - n_{i,0})\Delta\mu_i$$

where ΔH_X is the formation enthalpy of the defective structure, ΔH_0 is the formation enthalpy of the pristine structure, n_i is the number of moles of element i, and $\Delta\mu_i$ is the deviation in the chemical potential of element i from its reference state. Ca vacancies (V_{Ca}) and Ca interstitials (Ca_i) were charge-compensated by O_N and N_O substitutional defects, respectively; therefore, all of the defects were charge-neutral. The defect formation energies were calculated in the chemical potential window where $Ca_3BaSi_{10}O_6N_{12}$ was found to be a stable phase (on the convex hull). The defect orderings were calculated in ~10−20 configurations with low electrostatic energy evaluated using the Ewald method implemented in pymatgen.[53]

AIMD Simulation. Ab initio molecular dynamics (AIMD) calculations were performed with the generalized gradient approximation (GGA), as implemented by Perdew, Burke, and Ernzerhof (PBE).[54] Each calculation was initialized with the lowest-energy configuration for each composition of interest. For the structures exhibiting Ca mobility (those with V_{Ca} and O_N defects), O is substituted for N in the Ba−N polyhedra and the compensating defect is thus farthest from the Ca−O channels where Ca is observed to be mobile. All of the AIMD calculations were performed in an NVT ensemble using a Nosé−Hoover thermostat[55] and a time step of 1 fs. A minimal Γ-point-only k-point grid and a plane-wave energy cutoff of 400 eV were used for these calculations with the same pseudopotentials, as described for the thermodynamic analysis. The calculations were performed at 600, 900, 1200, and 1500 K and terminated prematurely if

negligible Ca mobility was observed after ~5−20 ps. AIMD trajectories were analyzed using pymatgen.[53,56]

RESULTS

Synthesis and Structural Characterization. CBSON was successfully synthesized via a conventional solid-state reaction at 1400 °C under a N_2 flow, with CaO, $Ca(OH)_2$, BaO, SiO_2, and Si_3N_4 as raw materials. The addition of $Ca(OH)_2$, a low-melting Ca source, promotes the diffusion of precursors, thereby accelerating the reaction and inhibiting impurity formation (e.g., $CaSi_2O_2N_2$). However, the use of excessive $Ca(OH)_2$ may lead to severe Ca loss considering the high reaction temperature. Therefore, a series of $CaO:Ca(OH)_2$ ratios were attempted, and the X-ray diffraction (XRD) patterns of reaction products (Figure S1) show that a 1:1 ratio of $Ca(OH)_2:CaO$ can form pure CBSON phase. Hence, this ratio of Ca source was used to create all samples in this study.

The crystal structure of CBSON with the *Cm* space group is shown in Figure 1a. The structure of the as-synthesized CBSON was confirmed by Rietveld refinement of time-of-flight neutron powder diffraction (NPD) data at 290 K, as shown in Figures 1b and S3. The low R factors of the refinement indicate a good fit to the structural model in Figure 1a, and no impurity peaks were observed. The resulting lattice parameters, atomic coordinates, site occupancies, and thermal displacement factors are

Table 1. Crystallographic Data of $Ca_{1.5}Ba_{0.5}Si_5O_3N_6$ as Obtained from Rietveld Refinement of Time-of-Flight NPD Data at 290 K[a]

space group	a (Å)	b (Å)		c (Å)	β (°)	V (Å³)
C1m1	7.0663(2)	23.9253(6)		4.8255(2)	109.427(2)	769.36(3)
atom	site	x	y	z	U_{iso} (Å²)	occupancy
Ba1	2a	0.9226(11)	0	0.1122(11)	0.0167(10)	1
Ca1	4b	0.5927(16)	0.7805(4)	0.511(2)	0.0228(12)	0.5
Ca2	4b	0.4336(17)	0.2497(3)	0.188(2)	0.0228(12)	0.5
Ca3	4b	0.7854(15)	0.7371(4)	0.8917(18)	0.0228(12)	0.5
Si1	4b	0.1576(6)	0.1255(2)	0.2463(8)	0.0015(2)	1
Si2	4b	0.9246(7)	0.1376(2)	0.6371(8)	0.0015(2)	1
Si3	4b	0.6800(6)	0.1331(2)	0.0108(9)	0.0015(2)	1
Si4	4b	0.2943(6)	0.0638(2)	0.8239(10)	0.0015(2)	1
Si5	4b	0.5501(6)	0.9347(2)	0.4485(9)	0.0015(2)	1
N1	4b	0.7063(3)	0.1140(1)	0.6787(5)	0.0029(1)	1
N2	2a	0.2116(4)	0	0.8408(8)	0.0140(4)	1
N3	4b	0.1279(3)	0.1112(1)	0.8873(4)	0.0029(1)	1
N4	4b	0.5354(2)	0.0788(2)	0.0876(4)	0.0029(1)	1
N5	4b	0.9179(4)	0.1223(1)	0.2790(5)	0.0029(1)	1
N6	4b	0.3126(3)	0.0798(2)	0.4803(5)	0.0029(1)	1
N7	2a	0.6321(5)	0	0.5533(8)	0.0140(4)	1
O1	4b	0.6019(5)	0.1958(2)	0.0233(9)	0.0137(8)	1
O2	4b	0.9281(5)	0.2074(1)	0.6795(7)	0.0073(5)	1
O3	4b	0.2357(6)	0.1924(2)	0.3232(8)	0.0111(7)	1

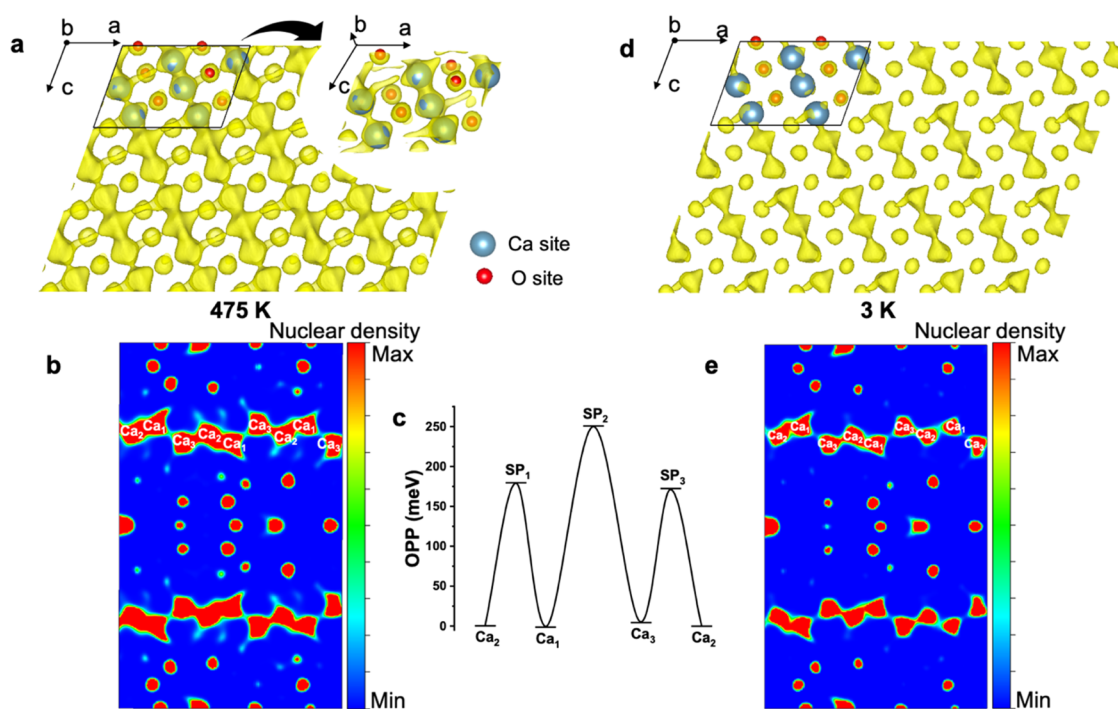[a]R_{wp} = 2.59%, R_p = 2.65%, and GOF = 2.87.

Figure 2. (a) Nuclear density isosurface plot obtained by an MEM analysis on the NPD data at 475 K shown in the Ca layer down the [010] direction (surface threshold, 0.03 fm/Å³). In the unit cell, Ca and O sites are shown as blue and red balls, respectively. The inset presents a slightly tilted isosurface view of the Ca layer. (b) Nuclear density map at 475 K sliced in the (232.11, 1, −110.309) plane with a distance from the origin of 2.47616 Å. (c) Effective one-particle potential profile along the 1D diffusion path, which is calculated from the nuclear density map at 475 K by assuming the validity of Boltzmann statistics. (d) Nuclear density isosurface plot at 3 K in the Ca layer down the [010] direction (surface threshold, 0.03 fm/Å³). (e) Nuclear density map at 3 K sliced in the (232.11, 1 −110.309) plane with a distance from the origin of 2.47616 Å. The scale is the same as in panel (b).

summarized in Table 1. There are three distinct half-occupied 4b Wyckoff sites for Ca, which constitute layers between SiX_4 (X = N, O) tetrahedral networks. Each Ca^{2+} in the layer is surrounded by six O^{2-} and one N^{3-}. The Ba ions occupy the large pores created by the vertex-sharing network of SiX_4 (X = N, O) tetrahedra and are coordinated by 12 N^{3-}. Figure 1c presents a high-angle annular dark-field (HAADF) scanning transmission electron microscopy (STEM) image of a CBSON particle. The
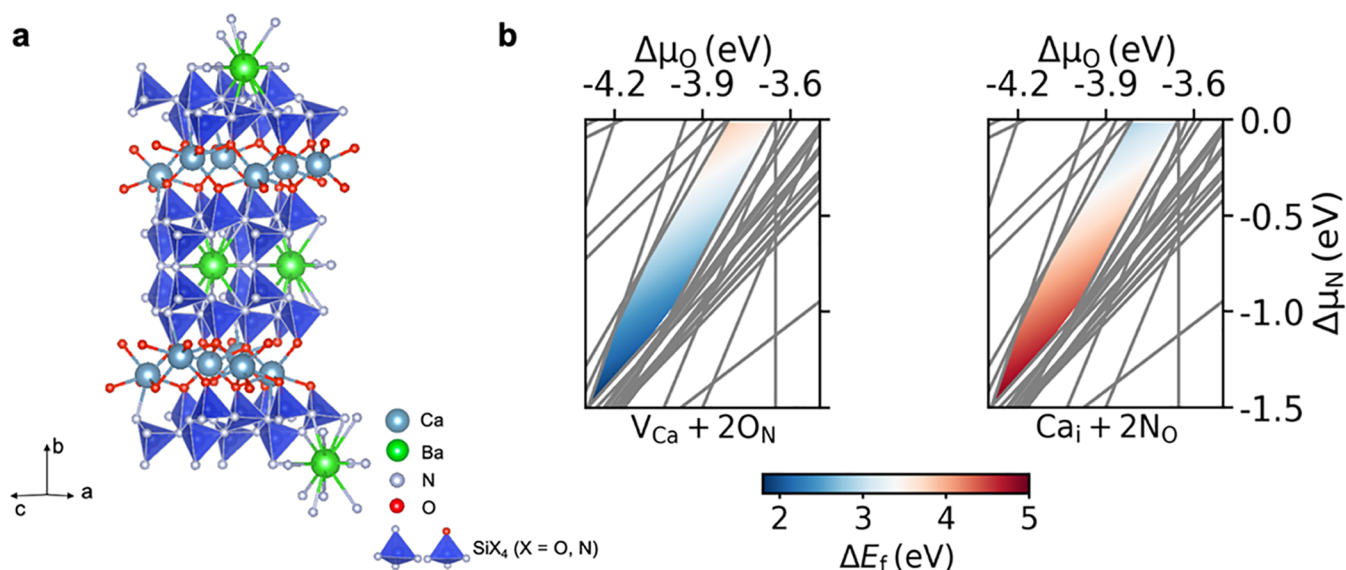
Figure 3. (a) Lowest-energy-ordered CBSON structure in a $1 \times 1 \times 2$ supercell from DFT calculation. (b) Formation energies of Ca vacancies (left) and Ca (right) interstitials in CBSON. $\Delta\mu_i$ is the chemical potential of species i relative to its elemental state, and values close to 0 indicate an i-rich atmosphere. Each gray line represents a stable competing compound in the Ca−Ba−Si−O−N chemical space. The colored region corresponds to the range of chemical potentials where CBSON is stable. The defect concentrations are $1/12\ V_{Ca}$, $1/24\ O_N$ on the left side and $1/12\ Ca_i$, $1/12\ N_O$ on the right side. The complete chemical potential triangle is shown in Figure S6.

corresponding energy-dispersive X-ray spectroscopy (EDS) elemental mapping reveals a uniform distribution of Ca, Ba, Si, O, and N without visible surface segregation or phase separation, which is consistent with the pure phase observed in the NPD. ICP-OES elemental analysis further confirmed that the cation ratios in the as-synthesized material are close to those of the target compositions (Table S1). The partial Ca occupancy and extremely short distances (1.727−2.077 Å) between neighboring Ca sites in the same layer suggest that high-energy Ca^{2+}-site occupation states may exist, implying the possibility of Ca-ion conduction via a concerted migration mechanism, as argued for several classic Li superionic conductors including $Li_{10}GeP_2S_{12}$ and $Li_7La_3Zr_2O_{12}$ (LLZO).[30]

Possible Ca Diffusion Pathways Identified by the Maximum Entropy Method. To identify the potential Ca diffusion pathways in CBSON, nuclear density maps were constructed using the maximum entropy method (MEM) on the NPD. MEM derives three-dimensional densities that maximize the information entropy, which can recover part of the structural information lost in powder diffraction.[57] Thus, MEM can provide less noisy 3D densities than conventional Fourier synthesis. Recently, MEM has emerged as a powerful technique to analyze likely diffusion paths in solid-state conductors.[58−60] The NPD patterns collected at 475 and 3 K are shown in Figure S4, and the structure parameters from Rietveld refinement are provided in Tables S2 and S3. Figure 2a presents the nuclear density isosurface plot of the Ca slab down the [010] direction at 475 K obtained from the MEM analysis. A continuous one-dimensional (1D) chain of nuclear density maxima that connects the three half-occupied Ca sites can be clearly identified at this selected isosurface threshold. The inset in Figure 2a presents a slightly tilted view of the nuclear density plot, from which it can be observed that the density branches from the main 1D chain are not connected across the 1D channels. In contrast, at the same isosurface threshold, the nuclear density around O, Ba, Si, and N ions is localized (Figure S5). In Figure 2b, a two-dimensional slice of the nuclear density

map collected at 475 K perpendicular to the Ca slab and parallel to a possible Ca diffusion channel is shown. The nuclear density in this view suggests that Ca^{2+} are considerably delocalized from their equilibrium sites along a Ca2−Ca1−Ca3−Ca2 pathway. The high nuclear density between Ca3−Ca2 and Ca2−Ca1 sites indicates a considerable probability of Ca occupying intermediate positions between these equilibrium sites, suggesting a potential pathway for Ca^{2+} hopping. The minimum nuclear density observed between the Ca1 and Ca3 sites suggests that this might be the bottleneck along the 1D diffusion path.

Both static and dynamic disorder can lead to nuclear density away from the equilibrium sites. To distinguish the scenarios, we performed the same NPD measurement at 3 K, and the resulting nuclear density distributions obtained with MEM are presented in Figure 2d,e. The diminished nuclear density and connectivity of Ca chains observed at this cryogenic temperature likely arise from the freezing out of the dynamic disorder of Ca^{2+}. However, a small amount of delocalization of the nuclear density around Ca sites remains at 3 K, indicating that some static disorder may also exist in this system.

To better quantify the potential Ca migration landscape, we used the nuclear density map as a probability density for Ca. By assuming the normalized nuclear density map to be a probability field and 475 K to be sufficiently high temperature to allow the application of Boltzmann statistics, it is possible to calculate the effective one-particle potential (OPP).[61] The activation energy of Ca-ion hopping between two adjacent sites can then be estimated from the equation $\rho_{sp} = \rho_0 \exp\left(-\frac{E_a}{k_B T}\right)$, where ρ_{sp} and ρ_0 are the observed probability density at the saddle point and equilibrium site, respectively,[62] as shown in Figure 2c. The resulting activation energies, E_a, for hopping between Ca2 and Ca1 and between Ca3 and Ca2 sites are remarkably low, ~179 and ~172 meV, respectively, whereas the Ca1−Ca3 hopping has a higher barrier of 250 meV. Thus, in this approximation, percolating 1D diffusion is governed by an energy barrier of ~250 meV. This value is an estimate, as in this approach, the ion
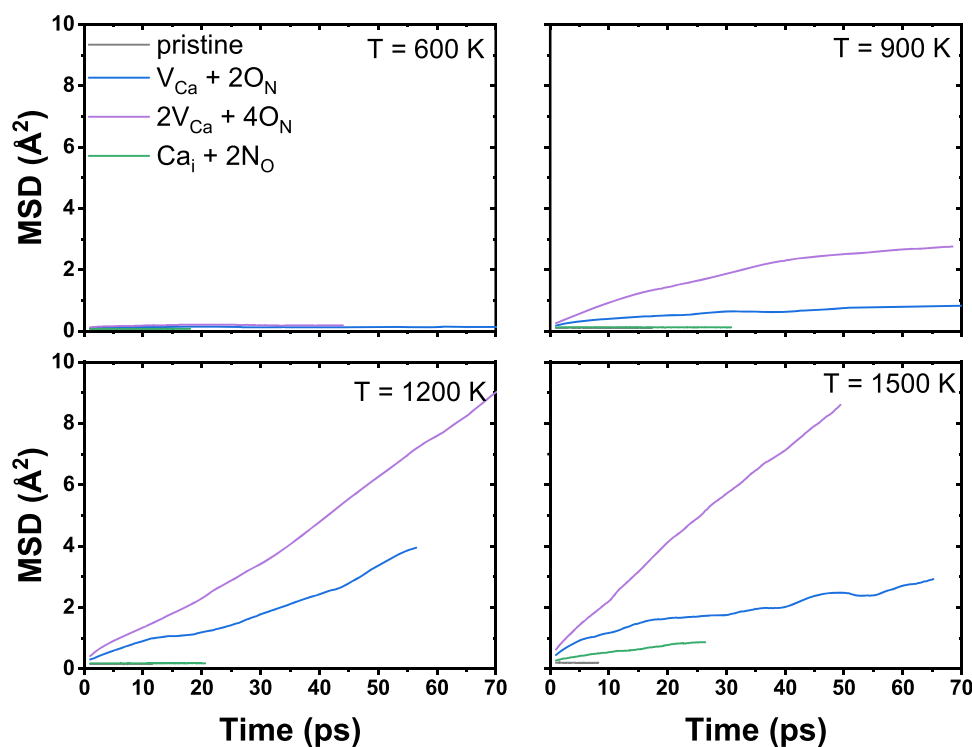
Figure 4. Mean square displacement (MSD) of Ca ion during AIMD simulation at 600, 900, 1200, and 1500 K. The pristine CBSON supercell and supercells with additional $1/12\ V_{Ca}$, $1/6\ V_{Ca}$, and $1/12\ Ca_i$ are shown as gray, blue, purple, and green lines, respectively. Note that configurations exhibiting effectively zero Ca mobility were cut short to reduce computational cost.

is treated individually within the classical limit, and the role of Ca−Ca interactions is only incorporated in a mean field way. This low-energy barrier along with the reported nuclear density maps nevertheless suggests the potential for facile Ca-ion conduction in CBSON. To investigate the possibility of Ca in a more quantitative way, we further evaluate the Ca migration barriers and possible point defects with ab initio calculations.

Computational Analysis of CBSON. First-principles DFT calculations were applied to better understand the thermodynamic and electrochemical stability, defect formation, and Ca mobility in CBSON. To investigate the Ca arrangement in the structure, 16 unique Ca configurations with low electrostatic energy in a $1 \times 1 \times 2$ supercell were calculated with DFT. The lowest-energy-ordered CBSON structure with half Ca sites fully occupied and half vacant features no nearest-neighbor Ca sites being simultaneously occupied, as shown in Figure 3a. This structure was used for subsequent calculations. The CBSON phase was calculated to be on the convex hull of stability in the Ca−Ba−Si−O−N chemical space, with a decomposition enthalpy $\Delta H_d = -26$ meV/atom relative to $Ca_2SiO_4 + CaSi_2O_2N_2 + BaSi_7N_{10}$. To calculate the electrochemical stability window of CBSON, a grand potential phase diagram[51] open to Ca was used and indicated that CBSON is stable from 1.2 to 4.0 V vs Ca/Ca^{2+}. The thermodynamic stability and relatively wide electrochemical stability window of CBSON make it potentially suitable as a solid-state electrolyte for Ca batteries.

To better quantify the Ca mobility, we first evaluated the possible point defects and their energy in CBSON as point defects are often required to enable ion diffusion. The formation energies for two types of Ca defects, vacancies (V_{Ca}) and interstitials (Ca_i), were calculated with substitutional defects on the anion sites (i.e., $2O_N$ per V_{Ca} or $2N_O$ per Ca_i) as charge

compensation. Because these defects change the composition of the compound, their formation energy depends on the external chemical potentials of species, $\Delta\mu$. To determine a suitable range of chemical potentials over which to evaluate defect formation energies, we used the "chemical potential triangle" approach.[63] In this approach, we first determine the range of chemical potentials where CBSON is thermodynamically stable. Because it is usually possible to exhibit control of the chemical potentials of gaseous species during synthesis, we performed this analysis as a function of $\Delta\mu_O$ and $\Delta\mu_N$. In Figure 3b, we show a subset of the complete chemical potential triangle (shown in Figure S6) and map the defect formation energy of Ca vacancies and interstitials with variable O and N chemical potentials in the region where CBSON is thermodynamically stable. Each gray line in the figure represents a stable competing compound in the Ca−Ba−Si−O−N chemical space. On the basis of these results, Ca vacancies are predicted to have formation energies ranging from ∼1.5 to 4 eV and are favored to form in nitrogen-poor conditions, whereas Ca interstitials are predicted to have much higher formation energies ranging from ∼3 to 5 eV and are favored to form in nitrogen-rich conditions. Therefore, Ca vacancies (with compensating O_N defects) appear more likely to form in CBSON than Ca interstitials (with compensating N_O defects). While in this work, we only considered charge compensation on the anion site, replacing Ba or Si with higher (lower) valent ions could also be a strategy to form Ca vacancies (interstitials).

AIMD simulations were further applied to probe the Ca-ion mobility in CBSON. In addition to the ordered pristine supercell featuring the lowest-energy Ca configuration, the supercells with either one Ca vacancy ($1/12\ V_{Ca}$), two Ca vacancies ($1/6\ V_{Ca}$), or one Ca interstitial ($1/12\ Ca_i$) were simulated at elevated temperatures. The mean square displacements of Ca^{2+} at 600,
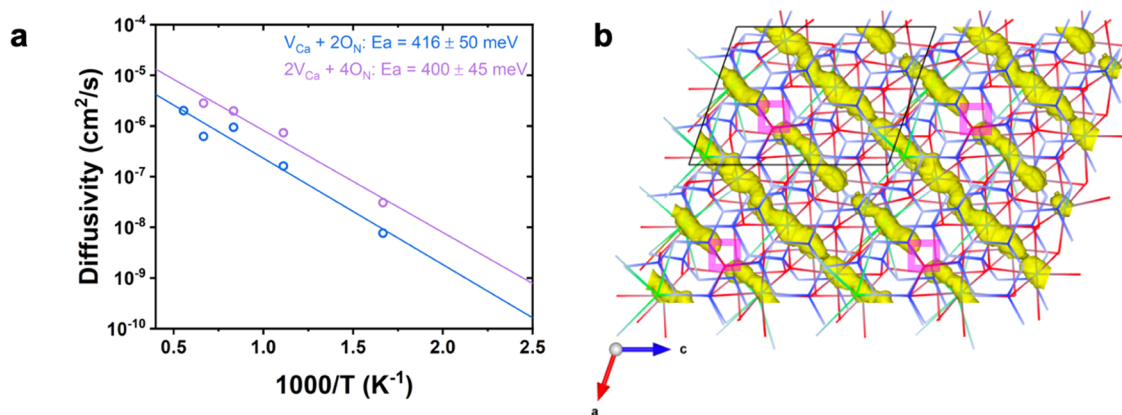
Figure 5. (a) Arrhenius plots of AIMD-calculated diffusivities with Ca vacancies introduced in CBSON. (b) Ca-ion probability density of CBSON with $1/12\,V_{Ca}$ from AIMD simulation at 1500 K down the [010] direction. The initial atomic positions are represented by the wireframe: green, Ba; blue, Si; red, O; purple, N; Ca is not shown. The Ca vacancy sites are marked by pink boxes.
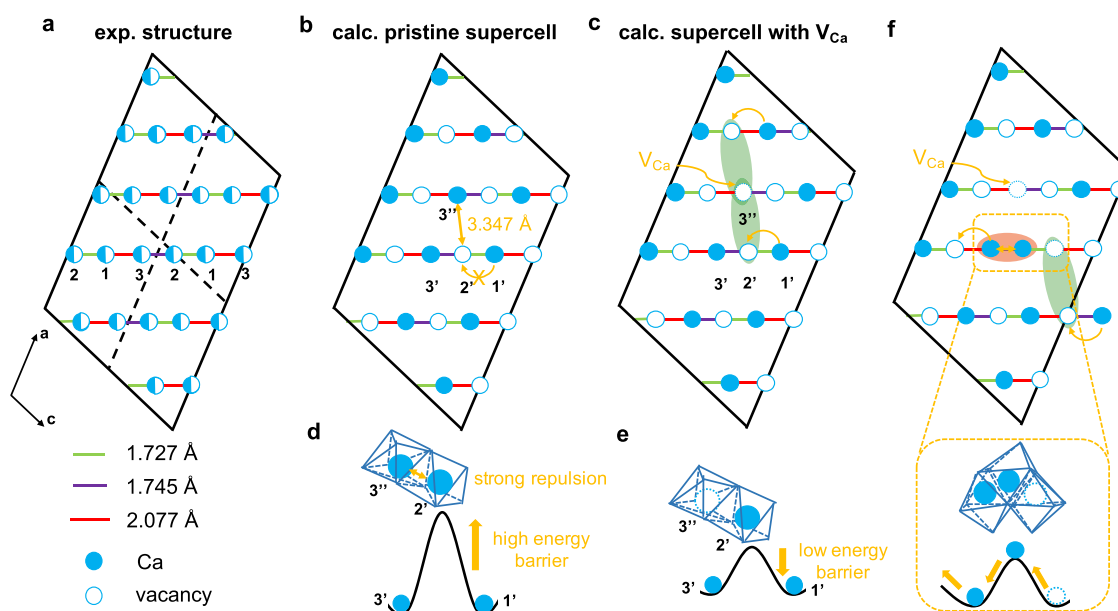

Figure 6. Schematic illustration of Ca ordering and site occupancies in CBSON down the [010] direction: (a) structure determined from NPD refinement, (b) calculated lowest-energy pristine supercell (inactive for Ca diffusion), and (c) calculated supercell with additional $1/12\,V_{Ca}$ (at position 3″), where Ca diffusion is activated in 1D channels adjacent to the vacancy ($1' \rightarrow 2' \rightarrow 3'$). Schematic illustrations of the energy landscape for Ca-ion migration are shown for the pristine supercell in panel (d) and the supercell with an additional $1/12\,V_{Ca}$ in panel (e). (f) Schematic illustration of concerted ion migration induced by the unique Ca^{2+} configuration and strong ion−ion interaction within the 1D channel adjacent to the channel that contains a static vacancy. The green-shaded region indicates the structural feature of "unoccupied face-sharing sites across channels", and the red-shaded region indicates the structural feature of "occupied neighboring sites in channels".

900, 1200, and 1500 K for each configuration are shown in Figure 4. In the pristine supercell and the one with a Ca interstitial, effectively zero displacement of Ca^{2+} is observed even at the highest simulation temperature of 1500 K. In contrast, Ca motion is clearly observed for supercells that contain Ca vacancies. These results suggest that Ca vacancies are required to activate Ca-ion diffusion in CBSON. For these supercells with Ca vacancies, the temperature-dependent diffusivity data exhibit Arrhenius behavior, as shown in Figure 5a. The resulting energy barriers for Ca diffusion derived from this Arrhenius analysis in CBSON supercells with $1/12\,V_{Ca}$ and $1/6\,V_{Ca}$ are 416 and 400 meV, respectively, which are among the lowest migration barriers reported for Ca^{2+} in solid-state materials.[4] The extrapolated Ca-ion conductivities at room temperature are 5.4×10^{-7} S/cm for $1/12\,V_{Ca}$ and 2.64×10^{-6}

S/cm for $1/6\,V_{Ca}$. We note that due to the small number of carriers, the present simulations do not always reach the Fickian diffusive regime where log(MSD) vs log(time) has a slope of unity,[64] so the derived activation barriers and conductivities should be taken as estimates. In Figure S7, we show the corresponding log−log plots, and in Figure S8, we show refittings of the Arrhenius analysis excluding the 600 K simulation that deviates most strongly from the Fickian diffusive regime, which result in activation energies of about 250 meV for the $2\,V_{Ca}$ system and 320 meV for the $1\,V_{Ca}$ system.

The Ca-ion probability density in the Ca layer extracted from the trajectory at 1500 K for the CBSON supercell with $1/12\,V_{Ca}$ is shown in Figure 5b. The connected 1D Ca-ion diffusion channel within the a−c plane can clearly be identified and is consistent with the pathway determined from the experimental

NPD and MEM analysis (Figure 2). Conventional vacancy-mediated cation diffusion involves the hopping of an ion into the vacancy, thereby migrating both the vacancy and the ion that moved. In CBSON, however, we find that the Ca vacancy remains mostly unoccupied during the period of AIMD simulation (sites marked by pink boxes in Figure 5b). Instead, we find substantial Ca diffusion in the 1D channels adjacent to the vacancy. This finding suggests that the formation of Ca vacancies in a given 1D channel facilitates Ca hopping in the adjacent channels. In these vacancy-adjacent channels, Ca-ion mobility may be facilitated by concerted hopping as a result of the very short distances between occupiable Ca sites. Therefore, we call this unexpected phenomenon a "vacancy-adjacent" concerted ion migration mechanism, as discussed in more detail in subsequent sections.

◼ DISCUSSION

"Vacancy-Adjacent" Concerted Ion Migration Mechanism. The fact that the vacancy itself is less mobile but instead induces mobility in the adjacent channels is to the best of our knowledge a novel mechanism. In Figure 6a−c, we present 2D sketches of the Ca sites in CBSON to better illustrate the nature of the "vacancy-adjacent" concerted ion migration pathway. In Figure 6a, all of the Ca sites are shown as partially occupied, in accordance with the Rietveld refinement of the NPD data. This provides an average picture in which each Ca site is half-occupied. The extremely short distances (1.727−2.077 Å) between the neighboring occupiable Ca sites along the 1D diffusion channel make it unlikely that two neighboring sites are simultaneously occupied. This is confirmed by our DFT calculations of various Ca/V_{Ca} orderings, indicating that the pristine unit cell shown in Figure 6b has the lowest energy at 0 K. The partial occupancy with which the experimental structure is refined may reflect the fact that the thermally induced disorder at high temperature does not equilibrate in the experimental sample when it is cooled, that very small domains of local Ca/V_{Ca} ordering with antiphase boundaries between them exist, or that simply too small a unit cell has been used for the refinement.

Our AIMD simulations indicate that additional Ca vacancies (beyond the unoccupied Ca sites arising from the half-occupancy, denoted as static vacancies) are needed to activate ion migration in CBSON. However, Ca vacancies play a different role than in conventional vacancy-mediated cation diffusion. In CBSON, the static vacancy appears to unlock the 1D diffusion pathways in adjacent channels. As shown in Figure 6d, in the ordered pristine supercell without static vacancies, the Ca ion needs to hop through an unoccupied site that is face-sharing with an occupied Ca site in the adjacent channel. The strong Ca−Ca repulsion results in a high-energy barrier when a Ca ion has to migrate through a site that face-shares with another occupied site. A static vacancy in an adjacent channel alleviates this high site energy by creating two unoccupied face-sharing sites across channels, as shown by the green shading in Figure 6c,e, activating Ca-ion diffusion to fill the unoccupied sites.

Within a 1D channel, once Ca^{2+} starts to migrate to a nearby unoccupied site, a unique Ca^{2+} configuration is created where nearest-neighbor Ca sites are temporarily occupied, as shown by the red shading in Figure 6f. Given the extremely short distance between the two sites, the strong Ca−Ca interaction is likely to induce concerted ion migration, during which the Ca ion at high-energy sites migrates downhill in energy, canceling out a part of the energy barrier felt by other uphill-climbing Ca ions. This activated concerted ion migration in the 1D channel leads

to the low-energy barrier for Ca-ion conduction. Such concerted mechanisms have been widely argued to explain the high ionic conductivity in many superionic conductors when interactions between mobile ions are significant.[30,65,66]

Furthermore, Ca hopping in this 1D channel creates newly unoccupied Ca sites and thus a local environment featuring unoccupied face-sharing sites across channels temporarily forms (Figure 6f). This may act similarly to the configuration created by the static vacancy to activate the concerted Ca-ion migration again in its adjacent channels, promoting Ca-ion conduction in additional diffusion channels. Indeed, as shown in Figure S9a−c, the channels that are not adjacent to the static vacancy do exhibit some Ca mobility, though the mobility is lower than that in the channel adjacent to the static vacancy as a lower isosurface threshold is required to make Ca-ion probability density fully connected in these channels. In contrast, for the same AIMD simulation, the layer that does not have any static vacancies exhibits only small displacements of Ca around the equilibrium positions for the same isosurface threshold (Figure S9d). The Ca mobility near the static vacancy is low because this static vacancy introduces three consecutive unoccupied Ca sites within its channel, which limits the concerted mechanism within this channel as the distance between occupied Ca sites is too large to hop (shown in Figure 6c) and no strong Ca−Ca interactions are present to assist diffusion. Nevertheless, the observation of mobile Ca in a channel that is not adjacent to a static vacancy does provide evidence that the creation of one static vacancy may activate Ca-ion diffusion beyond its two adjacent channels. Because the unoccupied face-sharing sites across channels that activate diffusion are created dynamically in channels that are not adjacent to a static vacancy, we can expect that Ca mobility in a channel decreases with increasing distance from the static vacancy.

To summarize, the important structural features that activate Ca-ion diffusion in CBSON are (1) unoccupied face-sharing sites across channels (green shading in Figure 6) or (2) occupied neighboring sites in channels (red shading in Figure 6). The "vacancy-adjacent" concerted ion migration observed in CBSON can be understood as follows: (1) static Ca vacancies are needed to create structural feature (1); (2) within the activated 1D channels, the initial Ca hop into one of these unoccupied sites leads to structural feature (2), creating a concerted ion diffusion mechanism for further hopping. This concerted ion motion can then travel in its channel until it meets an existing static vacancy that annihilates it. (3) Structural feature (1) can be temporarily created by Ca hopping in channels exhibiting diffusion; thus, it is plausible that Ca-ion diffusion by a similar mechanism is promoted in new adjacent channels. As a result, one static vacancy activates Ca-ion diffusion in more than its two adjacent channels, and the minimum concentration of Ca vacancies required to activate percolating Ca-ion conduction should be relatively low. However, the probability of concerted Ca hopping (structural feature (2)) in the vicinity of the static vacancy is low, limiting mobility in the channel containing the static vacancy. In our AIMD simulations, we do observe some finite occupation of the initial static vacancy by Ca (Figure S9c), indicating that these static vacancies do not completely stop diffusion in those channels. Nevertheless, considering that these static vacancies can result in diffusion bottlenecks, high Ca vacancy concentrations should be avoided. The percolating 1D diffusion channel shown in the nuclear density map from neutron
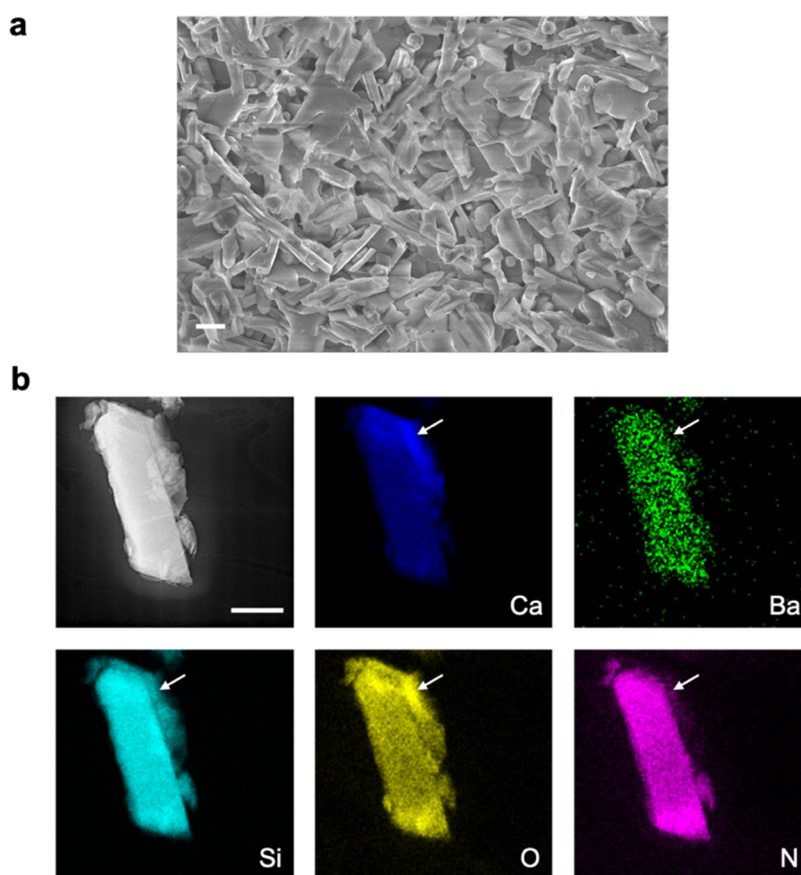
Figure 7. (a) Cross-sectional SEM image of the as-synthesized CBSON pellet. Scale bar: 2 μm. (b) HAADF image of CBSON particle after resintering at 1400 °C for 5 h and corresponding EDS mapping acquired from STEM. Scale bar, 400 nm.

diffraction (Figure 2) may therefore arise from a small amount of V_{Ca} point defects in the as-synthesized CBSON.

The unique migration mechanism observed here suggests that the interactions between mobile ions play an important role in solid-state ion diffusion for multivalent-ion systems. Furthermore, the diffusion of large cations (e.g., Ca^{2+}) in solid-state materials can be more complex than that of small cations (e.g., Li^+). The larger cation size imposes additional constraints on the types of environments that can activate diffusion, and factors such as steric effects must be considered in the design of large-ion conductors. Here, these steric effects are accommodated by the vacancy-adjacent diffusion mechanism, in contrast to the traditional vacancy-mediated cation diffusion that is usually observed in solid-state ion conductors.

Challenges in Pellet Densification for CBSON. Both the nuclear density map from NPD/MEM analysis and AIMD simulation indicate that facile Ca-ion conduction in CBSON with a remarkably low migration barrier may be possible. To achieve reliable ionic conductivity measurement from electrochemical impedance spectroscopy (EIS), dense pellets are required to ensure interparticle contact and mitigate grain-boundary resistance. However, pellet densification can be very challenging, especially for hard and brittle refractory materials (e.g., oxides and nitrides). The highest relative pellet density we were able to achieve for the CBSON compound was very low (~60%), precluding the observation of ionic conductivity by EIS. Indeed, even for Li superionic conductors such as LLZO, such a low pellet density results in very poor measured ionic conductivity.[67,68] A cross-sectional SEM image of the as-synthesized CBSON pellet is shown in Figure 7a, from which

it can be observed that the particle size is relatively small (several μm) and that many particles are disconnected, consistent with high porosity. Such a porous microstructure impedes macroscopic Ca-ion conduction, especially for a 1D conductor where ion migration paths are vulnerable to being blocked.[69,70]

Resintering after synthesis is a conventional method to obtain densified conductor pellets for conductivity measurement. However, a post-synthesis sintering step at high temperatures (above 1300 °C) always led to decomposition of the CBSON compound. As shown in Figure 7b, after resintering, phase segregation can be clearly observed in the EDS mapping, as the elemental distributions are no longer homogeneous, especially for Ca, O, and N. This is very different from the EDS mapping of the as-synthesized CBSON sample (Figure 1c), where all of the elements are distributed homogeneously throughout the particle. Specifically, in the resintered samples, Ca tended to be concentrated in a small region where O was rich and N was almost not present. Thus, we speculate that calcium silicate may have formed as an impurity phase. Sintering at lower temperatures (below 1300 °C) did not improve the pellet density at all. Therefore, achieving a sufficiently high pellet density is quite challenging for CBSON and is the bottleneck preventing evaluation of the predicted Ca-ion conductivity by EIS measurements. Advanced sintering techniques need to be explored to densify CBSON pellets at lower temperatures. For example, spark plasma sintering or hot pressing have been studied as effective methods for densifying oxide-based Li superionic conductors,[68,71,72] which may also be helpful for CBSON. Other possible routes may be single crystal growth,

e.g., in a floating zone furnace, and single-particle measurements using microprobes.

CONCLUSIONS

In summary, we studied a potential Ca-ion conductor $Ca_{1.5}Ba_{0.5}Si_5O_3N_6$ (CBSON) by combining NPD/MEM analysis and AIMD simulations. CBSON was shown to contain percolating 1D Ca diffusion pathways with a remarkably low migration barrier between ∼250 meV (estimated from MEM analysis) and ∼400 meV (calculated by AIMD). The partially occupied Ca sites separated by short distances (1.727−2.077 Å) in CBSON trigger the unique "vacancy-adjacent" concerted ion migration mechanism, responsible for the low Ca migration barrier. CBSON is also predicted to have a relatively wide electrochemical stability window (1.2−4.0 V vs Ca/Ca^{2+}), making it an interesting candidate as a solid-state electrolyte for Ca batteries.

This work provides a new understanding of Ca-ion migration in solid-state materials, which is important for the future design of fast multivalent-ion conductors. Specifically, size and electrostatic interactions between mobile ions are significant and can greatly affect multivalent-ion migration. The large size of Ca imposes additional constraints on ion diffusion and leads to the unique "vacancy-adjacent" concerted ion migration mechanism observed here, which has not been found in the diffusion of small cations (e.g., Li). Unlike most vacancy-mediated ion migration mechanisms, for CBSON, the vacancy itself is rarely transported during diffusion but instead provides space to activate concerted migration in the 1D channels adjacent to the vacancy.

The main challenge to realizing the intrinsic Ca-ion conductivity in CBSON experimentally is pellet densification. Future work should explore the use of advanced sintering procedures (e.g., spark plasma sintering, hot pressing, flash sintering) or characterization techniques (e.g., single-particle measurements) to enable the observation of Ca-ion conductivity in CBSON.

ASSOCIATED CONTENT

ⓢ Supporting Information

The Supporting Information is available free of charge at https://pubs.acs.org/doi/10.1021/acs.chemmater.1c02923.

> XRD of products synthesized by different precursors and different ball mill materials; additional time-of-flight NPD data with Rietveld refinement; Rietveld refinement results of NPD at 475 and 3 K; additional nuclear density isosurface plots; full chemical potential triangle for CBSON; log−log plots of MSD vs time from AIMD simulation; additional Arrhenius plots fit to AIMD data; Ca-ion probability density of CBSON from AIMD with different isosurface thresholds; and ICP-OES elemental analysis results (PDF)

> Crystallographic Information File of CBSON from time-of-flight NPD refinement (CIF)

AUTHOR INFORMATION

Corresponding Authors

Huiwen Ji − *Energy Storage and Distributed Resources Division, Lawrence Berkeley National Laboratory, Berkeley, California 94720, United States; Department of Materials Science and Engineering, The University of Utah, Salt Lake City, Utah 84112, United States;* Email: huiwen.ji@utah.edu

Gerbrand Ceder − *Department of Materials Science and Engineering, University of California, Berkeley, Berkeley, California 94720, United States; Materials Sciences Division, Lawrence Berkeley National Laboratory, Berkeley, California 94720, United States;* ⓞ orcid.org/0000-0001-9275-3605; Email: gceder@berkeley.edu

Authors

Yu Chen − *Department of Materials Science and Engineering, University of California, Berkeley, Berkeley, California 94720, United States; Materials Sciences Division, Lawrence Berkeley National Laboratory, Berkeley, California 94720, United States;* ⓞ orcid.org/0000-0002-5420-7571

Christopher J. Bartel − *Department of Materials Science and Engineering, University of California, Berkeley, Berkeley, California 94720, United States; Materials Sciences Division, Lawrence Berkeley National Laboratory, Berkeley, California 94720, United States;* ⓞ orcid.org/0000-0002-5198-5036

Maxim Avdeev − *Australian Nuclear Science and Technology Organisation, Kirrawee DC, NSW 2232, Australia; School of Chemistry, The University of Sydney, Sydney, NSW 2006, Australia;* ⓞ orcid.org/0000-0003-2366-5809

Ya-Qian Zhang − *Department of Materials Science and Engineering, University of California, Berkeley, Berkeley, California 94720, United States; The Molecular Foundry, Lawrence Berkeley National Laboratory, Berkeley, California 94720, United States*

Jue Liu − *Neutron Scattering Division, Oak Ridge National Laboratory, Oak Ridge, Tennessee 37831, United States;* ⓞ orcid.org/0000-0002-4453-910X

Peichen Zhong − *Department of Materials Science and Engineering, University of California, Berkeley, Berkeley, California 94720, United States; Materials Sciences Division, Lawrence Berkeley National Laboratory, Berkeley, California 94720, United States;* ⓞ orcid.org/0000-0003-1921-1628

Guobo Zeng − *Department of Materials Science and Engineering, University of California, Berkeley, Berkeley, California 94720, United States; Materials Sciences Division, Lawrence Berkeley National Laboratory, Berkeley, California 94720, United States*

Zijian Cai − *Department of Materials Science and Engineering, University of California, Berkeley, Berkeley, California 94720, United States; Materials Sciences Division, Lawrence Berkeley National Laboratory, Berkeley, California 94720, United States;* ⓞ orcid.org/0000-0002-4908-3180

Haegyeom Kim − *Materials Sciences Division, Lawrence Berkeley National Laboratory, Berkeley, California 94720, United States;* ⓞ orcid.org/0000-0002-5962-8244

Complete contact information is available at: https://pubs.acs.org/10.1021/acs.chemmater.1c02923

Notes

The authors declare no competing financial interest.

ACKNOWLEDGMENTS

■ REFERENCES

(1) Muldoon, J.; Bucur, C. B.; Gregory, T. Quest for nonaqueous multivalent secondary batteries: magnesium and beyond. *Chem. Rev.* **2014**, *114*, 11683−11720.

(2) Canepa, P.; Sai Gautam, G.; Hannah, D. C.; Malik, R.; Liu, M.; Gallagher, K. G.; Persson, K. A.; Ceder, G. Odyssey of Multivalent Cathode Materials: Open Questions and Future Challenges. *Chem. Rev.* **2017**, *117*, 4287−4341.

(3) Tian, Y.; Zeng, G.; Rutt, A.; Shi, T.; Kim, H.; Wang, J.; Koettgen, J.; Sun, Y.; Ouyang, B.; Chen, T.; Lun, Z.; Rong, Z.; Persson, K.; Ceder, G. Promises and Challenges of Next-Generation "Beyond Li-ion" Batteries for Electric Vehicles and Grid Decarbonization. *Chem. Rev.* **2021**, *121*, 1623−1669.

(4) Arroyo-de Dompablo, M. E.; Ponrouch, A.; Johansson, P.; Palacin, M. R. Achievements, Challenges, and Prospects of Calcium Batteries. *Chem. Rev.* **2020**, *120*, 6331−6357.

(5) Gummow, R. J.; Vamvounis, G.; Kannan, M. B.; He, Y. Calcium-Ion Batteries: Current State-of-the-Art and Future Perspectives. *Adv. Mater.* **2018**, *30*, No. 1801702.

(6) Liu, M.; Jain, A.; Rong, Z.; Qu, X.; Canepa, P.; Malik, R.; Ceder, G.; Persson, K. A. Evaluation of sulfur spinel compounds for multivalent battery cathode applications. *Energy Environ. Sci.* **2016**, *9*, 3201−3209.

(7) Rong, Z.; Malik, R.; Canepa, P.; Sai Gautam, G.; Liu, M.; Jain, A.; Persson, K.; Ceder, G. Materials Design Rules for Multivalent Ion Mobility in Intercalation Structures. *Chem. Mater.* **2015**, *27*, 6016−6021.

(8) Gautam, G. S.; Canepa, P.; Malik, R.; Liu, M.; Persson, K.; Ceder, G. First-principles evaluation of multi-valent cation insertion into orthorhombic V2O5. *Chem. Commun.* **2015**, *51*, 13619−13622.

(9) Park, H.; Cui, Y.; Kim, S.; Vaughey, J. T.; Zapol, P. Ca Cobaltites as Potential Cathode Materials for Rechargeable Ca-Ion Batteries: Theory and Experiment. *J. Phys. Chem. C* **2020**, *124*, 5902−5909.

(10) Tchitchekova, D. S.; Ponrouch, A.; Verrelli, R.; Broux, T.; Frontera, C.; Sorrentino, A.; Bardé, F.; Biskup, N.; Arroyo-de Dompablo, M. E.; Palacín, M. R. Electrochemical Intercalation of Calcium and Magnesium in TiS2: Fundamental Studies Related to Multivalent Battery Applications. *Chem. Mater.* **2018**, *30*, 847−856.

(11) Arroyo-de Dompablo, M. E.; Krich, C.; Nava-Avendaño, J.; Palacín, M. R.; Bardé, F. In quest of cathode materials for Ca ion batteries: the CaMO 3 perovskites (M= Mo, Cr, Mn, Fe, Co, and Ni). *Phys. Chem. Chem. Phys.* **2016**, *18*, 19966−19972.

(12) Dompablo, M. E. A.-d.; Krich, C.; Nava-Avendaño, J.; Biškup, N.; Palacin, M. R.; Bardé, F. A joint computational and experimental evaluation of CaMn2O4 polymorphs as cathode materials for Ca ion batteries. *Chem. Mater.* **2016**, *28*, 6886−6893.

(13) Park, H.; Zapol, P. Thermodynamic and kinetic properties of layered-CaCo2O4 for the Ca-ion batteries: a systematic first-principles study. *J. Mater. Chem. A* **2020**, *8*, 21700−21710.

(14) Ponrouch, A.; Frontera, C.; Bardé, F.; Palacín, M. R. Towards a calcium-based rechargeable battery. *Nat. Mater.* **2016**, *15*, 169−172.

(15) Wang, D.; Gao, X.; Chen, Y.; Jin, L.; Kuss, C.; Bruce, P. G. Plating and stripping calcium in an organic electrolyte. *Nat. Mater.* **2018**, *17*, 16−20.

(16) Li, Z. Y.; Fuhr, O.; Fichtner, M.; Zhao-Karger, Z. Towards stable and efficient electrolytes for room-temperature rechargeable calcium batteries. *Energy Environ. Sci.* **2019**, *12*, 3496−3501.

(17) Seevers, R.; de Nuzzio, J.; Farrington, G. C.; Dunn, B. Ion transport in Ca2+, Sr2+, Ba2+, and Pb2+ beta″ aluminas. *J. Solid State Chem.* **1983**, *50*, 146−152.

(18) Nomura, K.; Ikeda, S.; Ito, K.; Einaga, H. Framework structure, phase transition, and transport properties in MIIZr4 (PO4) 6 compounds (MII= Mg, Ca, Sr, Ba, Mn, Co, Ni, Zn, Cd, and Pb). *Bull. Chem. Soc. Jpn.* **1992**, *65*, 3221−3227.

(19) Ikeda, S.; Takahashi, M.; Ishikawa, J.; Ito, K. Solid electrolytes with multivalent cation conduction. 1. Conducting species in Mg-Zr-PO4 system. *Solid State Ionics* **1987**, *23*, 125−129.

(20) Tamura, S.; Yamane, M.; Hoshino, Y.; Imanaka, N. Highly conducting divalent Mg2+ cation solid electrolytes with well-ordered three-dimensional network structure. *J. Solid State Chem.* **2016**, *235*, 7−11.

(21) Jaschin, P. W.; Gao, Y.; Li, Y.; Bo, S.-H. A materials perspective on magnesium-ion-based solid-state electrolytes. *J. Mater. Chem. A* **2020**, *8*, 2875−2897.

(22) Higashi, S.; Miwa, K.; Aoki, M.; Takechi, K. A novel inorganic solid state ion conductor for rechargeable Mg batteries. *Chem. Commun.* **2014**, *50*, 1320−1322.

(23) Roedern, E.; Kühnel, R.-S.; Remhof, A.; Battaglia, C. Magnesium ethylenediamine borohydride as solid-state electrolyte for magnesium batteries. *Sci. Rep.* **2017**, *7*, No. 46189.

(24) Canepa, P.; Bo, S.-H.; Sai Gautam, G.; Key, B.; Richards, W. D.; Shi, T.; Tian, Y.; Wang, Y.; Li, J.; Ceder, G. High magnesium mobility in ternary spinel chalcogenides. *Nat. Commun.* **2017**, *8*, No. 1759.

(25) Deyneko, D. V.; Petrova, D. A.; Aksenov, S. M.; Stefanovich, S. Y.; Baryshnikova, O. V.; Fedotov, S. S.; Burns, P. C.; Kosmyna, M. B.; Shekhovtsov, A. N.; Lazoryak, B. I. Ferroelectricity, ionic conductivity and structural paths for large cation migration in Ca10.5−xPbx(VO4)7 single crystals, x = 1.9, 3.5, 4.9. *CrystEngComm* **2019**, *21*, 1309−1319.

(26) Stefanovich, S. Y.; Petrova, D. A.; Morozov, V. A.; Fortalnova, E. A.; Belov, D. A.; Deyneko, D. V.; Barishnikova, O. V.; Belik, A. A.; Lazoryak, B. I. Enhanced nonlinear optical activity and Ca2+-conductivity in Ca10.5-xPbx(VO4)7 ferroelectrics. *J. Alloys Compd.* **2018**, *735*, 1826−1837.

(27) Koettgen, J.; Bartel, C. J.; Shen, J.-X.; Persson, K. A.; Ceder, G. First-principles study of CaB 12 H 12 as a potential solid-state conductor for Ca. *Phys. Chem. Chem. Phys.* **2020**, *22*, 27600−27604.

(28) Kamaya, N.; Homma, K.; Yamakawa, Y.; Hirayama, M.; Kanno, R.; Yonemura, M.; Kamiyama, T.; Kato, Y.; Hama, S.; Kawamoto, K.; Mitsui, A. A lithium superionic conductor. *Nat. Mater.* **2011**, *10*, 682−686.

(29) Murugan, R.; Thangadurai, V.; Weppner, W. Fast Lithium Ion Conduction in Garnet-Type Li7La3Zr2O12. *Angew. Chem., Int. Ed.* **2007**, *46*, 7778−7781.

(30) He, X.; Zhu, Y.; Mo, Y. Origin of fast ion diffusion in super-ionic conductors. *Nat. Commun.* **2017**, *8*, No. 15893.

(31) Park, W. B.; Singh, S. P.; Yoon, C.; Sohn, K.-S. Combinatorial chemistry of oxynitride phosphors and discovery of a novel phosphor for use in light emitting diodes, Ca1.5Ba0.5Si5N6O3:Eu2+. *J. Mater. Chem. C* **2013**, *1*, 1832−1839.

(32) Park, W. B.; Kim, H.; Park, H.; Yoon, C.; Sohn, K.-S. The Composite Structure and Two-Peak Emission Behavior of a Ca1.5Ba0.5Si5O3N6:Eu2+ Phosphor. *Inorg. Chem.* **2016**, *55*, 2534−2543.

(33) Neuefeind, J.; Feygenson, M.; Carruth, J.; Hoffmann, R.; Chipley, K. K. The nanoscale ordered materials diffractometer NOMAD at the spallation neutron source SNS. *Nucl. Instrum. Methods Phys. Res., Sect. B* **2012**, *287*, 68−75.

(34) Calder, S.; An, K.; Boehler, R.; Dela Cruz, C. R.; Frontzek, M. D.; Guthrie, M.; Haberl, B.; Huq, A.; Kimber, S. A.; Liu, J.; et al. A suite-level review of the neutron powder diffraction instruments at Oak Ridge National Laboratory. *Rev. Sci. Instrum.* **2018**, *89*, No. 092701.

(35) Rietveld, H. M. A profile refinement method for nuclear and magnetic structures. *J. Appl. Crystallogr.* **1969**, *2*, 65−71.

(36) Coelho, A. A. TOPAS and TOPAS-Academic: an optimization program integrating computer algebra and crystallographic objects written in C. *J. Appl. Crystallogr.* **2018**, *51*, 210−218.

(37) Ikeda, S.; Carpenter, J. M. Wide-energy-range, high-resolution measurements of neutron pulse shapes of polyethylene moderators. *Nucl. Instrum. Methods Phys. Res., Sect. A* **1985**, *239*, 536−544.

(38) Avdeev, M.; Hester, J. R. ECHIDNA: a decade of high-resolution neutron powder diffraction at OPAL. *J. Appl. Crystallogr.* **2018**, *51*, 1597−1604.

(39) Izumi, F.; Momma, K. Three-Dimensional Visualization in Powder Diffraction. In *Solid State Phenomena*; Trans Tech Publications, 2007; pp 15−20.

(40) Momma, K.; Ikeda, T.; Belik, A. A.; Izumi, F. Dysnomia, a computer program for maximum-entropy method (MEM) analysis and its performance in the MEM-based pattern fitting. *Powder Diffr.* **2013**, *28*, 184−193.

(41) Momma, K.; Izumi, F. VESTA 3 for three-dimensional visualization of crystal, volumetric and morphology data. *J. Appl. Crystallogr.* **2011**, *44*, 1272−1276.

(42) Kresse, G.; Joubert, D. From ultrasoft pseudopotentials to the projector augmented-wave method. *Phys. Rev. B* **1999**, *59*, 1758−1775.

(43) Blöchl, P. E. Projector augmented-wave method. *Phys. Rev. B* **1994**, *50*, 17953−17979.

(44) Kresse, G.; Furthmüller, J. Efficiency of ab-initio total energy calculations for metals and semiconductors using a plane-wave basis set. *Comput. Mater. Sci.* **1996**, *6*, 15−50.

(45) Kresse, G.; Furthmüller, J. Efficient iterative schemes for ab initio total-energy calculations using a plane-wave basis set. *Phys. Rev. B* **1996**, *54*, 11169−11186.

(46) Sun, J.; Ruzsinszky, A.; Perdew, J. P. Strongly Constrained and Appropriately Normed Semilocal Density Functional. *Phys. Rev. Lett.* **2015**, *115*, No. 036402.

(47) Yang, J. H.; Kitchaev, D. A.; Ceder, G. Rationalizing accurate structure prediction in the meta-GGA SCAN functional. *Phys. Rev. B* **2019**, *100*, No. 035132.

(48) Zhang, Y.; Kitchaev, D. A.; Yang, J.; Chen, T.; Dacek, S. T.; Sarmiento-Pérez, R. A.; Marques, M. A. L.; Peng, H.; Ceder, G.; Perdew, J. P.; Sun, J. Efficient first-principles prediction of solid stability: Towards chemical accuracy. *npj Comput. Mater.* **2018**, *4*, No. 9.

(49) Bartel, C. J.; Weimer, A. W.; Lany, S.; Musgrave, C. B.; Holder, A. M. The role of decomposition reactions in assessing first-principles predictions of solid stability. *npj Comput. Mater.* **2019**, *5*, No. 4.

(50) Jain, A.; Ong, S. P.; Hautier, G.; Chen, W.; Richards, W. D.; Dacek, S.; Cholia, S.; Gunter, D.; Skinner, D.; Ceder, G.; Persson, K. A. Commentary: The Materials Project: A materials genome approach to accelerating materials innovation. *APL Mater.* **2013**, *1*, No. 011002.

(51) Ong, S. P.; Wang, L.; Kang, B.; Ceder, G. Li−Fe−P−O2 Phase Diagram from First Principles Calculations. *Chem. Mater.* **2008**, *20*, 1798−1807.

(52) Freysoldt, C.; Grabowski, B.; Hickel, T.; Neugebauer, J.; Kresse, G.; Janotti, A.; Van de Walle, C. G. First-principles calculations for point defects in solids. *Rev. Mod. Phys.* **2014**, *86*, 253−305.

(53) Ong, S. P.; Richards, W. D.; Jain, A.; Hautier, G.; Kocher, M.; Cholia, S.; Gunter, D.; Chevrier, V. L.; Persson, K. A.; Ceder, G. Python Materials Genomics (pymatgen): A robust, open-source python library for materials analysis. *Comput. Mater. Sci.* **2013**, *68*, 314−319.

(54) Perdew, J. P.; Burke, K.; Ernzerhof, M. Generalized Gradient Approximation Made Simple. *Phys. Rev. Lett.* **1996**, *77*, 3865−3868.

(55) Nosé, S. A unified formulation of the constant temperature molecular dynamics methods. *J. Chem. Phys.* **1984**, *81*, 511−519.

(56) Deng, Z.; Zhu, Z.; Chu, I.-H.; Ong, S. P. Data-Driven First-Principles Methods for the Study and Design of Alkali Superionic Conductors. *Chem. Mater.* **2017**, *29*, 281−288.

(57) Izumi, F.; Momma, K. Three-dimensional visualization of electron-and nuclear-density distributions in inorganic materials by MEM-based technology. *IOP Conf. Ser.: Mater. Sci. Eng.* **2011**, *18*, No. 022001.

(58) Zhang, Z.; Roy, P. N.; Li, H.; Avdeev, M.; Nazar, L. F. Coupled Cation-Anion Dynamics Enhances Cation Mobility in Room-Temperature Superionic Solid-State Electrolytes. *J. Am. Chem. Soc.* **2019**, *141*, 19360−19372.

(59) Weber, D. A.; Senyshyn, A.; Weldert, K. S.; Wenzel, S.; Zhang, W.; Kaiser, R.; Berendts, S.; Janek, J.; Zeier, W. G. Structural Insights and 3D Diffusion Pathways within the Lithium Superionic Conductor Li10GeP2S12. *Chem. Mater.* **2016**, *28*, 5905−5915.

(60) Han, J.; Zhu, J.; Li, Y.; Yu, X.; Wang, S.; Wu, G.; Xie, H.; Vogel, S. C.; Izumi, F.; Momma, K.; Kawamura, Y.; Huang, Y.; Goodenough, J. B.; Zhao, Y. Experimental visualization of lithium conduction pathways in garnet-type Li7La3Zr2O12. *Chem. Commun.* **2012**, *48*, 9840−9842.

(61) Boysen, H. The determination of anharmonic probability densities from static and dynamic disorder by neutron powder diffraction. *Z. Kristallogr. − Cryst. Mater.* **2003**, *218*, 123−131.

(62) Cava, R.; Reidinger, F.; Wuensch, B. Single-crystal neutron diffraction study of the fast-ion conductor β-Ag2S between 186 and 325 °C. *J. Solid State Chem.* **1980**, *31*, 69−80.

(63) Zhang, S. B.; Wei, S.-H.; Zunger, A.; Katayama-Yoshida, H. Defect physics of the ${\mathrm{CuInSe}}_{2}$ chalcopyrite semiconductor. *Phys. Rev. B* **1998**, *57*, 9642−9656.

(64) He, X.; Zhu, Y.; Epstein, A.; Mo, Y. Statistical variances of diffusional properties from ab initio molecular dynamics simulations. *npj Comput. Mater.* **2018**, *4*, No. 18.

(65) Zou, Z.; Ma, N.; Wang, A.; Ran, Y.; Song, T.; Jiao, Y.; Liu, J.; Zhou, H.; Shi, W.; He, B.; Wang, D.; Li, Y.; Avdeev, M.; Shi, S. Relationships Between Na+ Distribution, Concerted Migration, and Diffusion Properties in Rhombohedral NASICON. *Adv. Energy Mater.* **2020**, *10*, No. 2001486.

(66) Jalem, R.; Yamamoto, Y.; Shiiba, H.; Nakayama, M.; Munakata, H.; Kasuga, T.; Kanamura, K. Concerted Migration Mechanism in the Li Ion Dynamics of Garnet-Type Li7La3Zr2O12. *Chem. Mater.* **2013**, *25*, 425−430.

(67) Rosero-Navarro, N. C.; Yamashita, T.; Miura, A.; Higuchi, M.; Tadanaga, K. Effect of Sintering Additives on Relative Density and Li-ion Conductivity of Nb-Doped Li7La3ZrO12 Solid Electrolyte. *J. Am. Ceram. Soc.* **2017**, *100*, 276−285.

(68) David, I. N.; Thompson, T.; Wolfenstine, J.; Allen, J. L.; Sakamoto, J. Microstructure and Li-Ion Conductivity of Hot-Pressed Cubic Li7La3Zr2O12. *J. Am. Ceram. Soc.* **2015**, *98*, 1209−1214.

(69) Morgan, D.; Van der Ven, A.; Ceder, G. Li Conductivity in Li[sub x]MPO[sub 4] (M = Mn, Fe, Co, Ni) Olivine Materials. *Electrochem. Solid-State Lett.* **2004**, *7*, A30.

(70) Malik, R.; Abdellahi, A.; Ceder, G. A Critical Review of the Li Insertion Mechanisms in LiFePO4Electrodes. *J. Electrochem. Soc.* **2013**, *160*, A3179−A3197.

(71) Baek, S.-W.; Lee, J.-M.; Kim, T. Y.; Song, M.-S.; Park, Y. Garnet related lithium ion conductor processed by spark plasma sintering for all solid state batteries. *J. Power Sources* **2014**, *249*, 197−206.

(72) Wolfenstine, J.; Allen, J.; Sumner, J.; Sakamoto, J. Electrical and mechanical properties of hot-pressed versus sintered LiTi2 (PO4)3. *Solid State Ionics* **2009**, *180*, 961−967.